

## MIT Open Access Articles

*THE DARK-MATTER FRACTION IN THE ELLIPTICAL  
GALAXY LENSING THE QUASAR PG 1115+080*

The MIT Faculty has made this article openly available. *Please share*  
how this access benefits you. Your story matters.

**Citation:** Pooley, D. et al. "THE DARK-MATTER FRACTION IN THE ELLIPTICAL GALAXY LENSING THE QUASAR PG 1115+080." *The Astrophysical Journal* 697.2 (2009): 1892. © 2009 The American Astronomical Society

**As Published:** <http://dx.doi.org/10.1088/0004-637X/697/2/1892>

**Publisher:** American Astronomical Society

**Persistent URL:** <http://hdl.handle.net/1721.1/52645>

**Version:** Final published version: final published article, as it appeared in a journal, conference proceedings, or other formally published context

**Terms of Use:** Article is made available in accordance with the publisher's policy and may be subject to US copyright law. Please refer to the publisher's site for terms of use.



THE DARK-MATTER FRACTION IN THE ELLIPTICAL GALAXY LENSING THE QUASAR  
PG 1115+080

This article has been downloaded from IOPscience. Please scroll down to see the full text article.

2009 ApJ 697 1892

(<http://iopscience.iop.org/0004-637X/697/2/1892>)

[The Table of Contents](#) and [more related content](#) is available

Download details:

IP Address: 18.51.1.222

The article was downloaded on 14/03/2010 at 22:13

Please note that [terms and conditions apply](#).

## THE DARK-MATTER FRACTION IN THE ELLIPTICAL GALAXY LENSING THE QUASAR PG 1115+080

D. POOLEY<sup>1</sup>, S. RAPPAPORT<sup>2</sup>, J. BLACKBURNE<sup>2</sup>, P. L. SCHECHTER<sup>2</sup>, J. SCHWAB<sup>2</sup>, AND J. WAMBSGANSS<sup>3,4</sup>

<sup>1</sup> Astronomy Department, University of Wisconsin–Madison, 475 North Charter Street, Madison, WI 53706, USA; [dave@astro.wisc.edu](mailto:dave@astro.wisc.edu)

<sup>2</sup> Department of Physics and Kavli Institute for Astrophysics and Space Research, MIT, Cambridge, MA 02139, USA

<sup>3</sup> Astronomisches Rechen-Institut, Zentrum für Astronomie der Universität Heidelberg, Moenchhofstr. 12-14, 69120 Heidelberg, Germany

<sup>4</sup> Bohdan Paczyński visitor, Princeton University Observatory, Princeton, NJ 08540, USA

Received 2008 August 24; accepted 2009 March 25; published 2009 May 15

### ABSTRACT

We determine the most likely dark-matter fraction in the elliptical galaxy quadruply lensing the quasar PG 1115+080 based on analyses of the X-ray fluxes of the individual images in 2000 and 2008. Between the two epochs, the  $A_2$  image of PG 1115+080 brightened relative to the other images by a factor of 6 in X-rays. We argue that the  $A_2$  image had been highly demagnified in 2000 by stellar microlensing in the intervening galaxy and has recently crossed a caustic, thereby creating a new pair of microimages and brightening in the process. Over the same period, the  $A_2$  image has brightened by a factor of only 1.2 in the optical. The most likely ratio of smooth material (dark matter) to clumpy material (stars) in the lensing galaxy to explain the observations is  $\sim 90\%$  of the matter in a smooth dark-matter component and  $\sim 10\%$  in stars.

*Key words:* dark matter – gravitational lensing – quasars: individual (PG1115+080)

### 1. INTRODUCTION

The theory of gravitational lensing is by now quite well understood (e.g., the reviews by Kochanek 2006; Wambsganss 2006). For the case of a quasar quadruply imaged by an intervening galaxy, a very simple model for the lensing potentials—a monopole plus a quadrupole—usually succeeds in fitting the positions of quasar images at the 1%–2% level. However, it has become increasingly clear that these same models do considerably worse at fitting the *relative fluxes* from quasar images (e.g., Kochanek & Dalal 2004; Metcalf & Zhao 2002). Such “flux ratio anomalies” are thought to be the product of small-scale structure in the gravitational potentials of the lensing galaxies.

There are two leading explanations for this small-scale structure. One intriguing explanation is that we are seeing *milli-lensing* by dark-matter condensations of subgalactic mass (Witt et al. 1995; Mao & Schneider 1998; Dalal & Kochanek 2002; Metcalf & Madau 2001; Chiba 2002), that are predicted in large numbers in  $N$ -body simulations. However, the much more likely explanation (and exciting for very different reasons) is that the flux ratio anomalies in the optical continuum and in X-rays are largely the result of *micro-lensing* by stars in the intervening galaxy (Witt et al. 1995; Schechter & Wambsganss 2002).

If the flux ratio anomalies are due to millilensing, i.e.,  $10^4$ – $10^8 M_\odot$  dark-matter condensations (Wambsganss & Paczyński 1992), then the Einstein radii of such masses, projected back to the quasar, are sufficiently large that we would expect the flux ratios to (1) be the same at all wavelengths, and (2) remain constant with time (except for source variability).

In fact, neither of these expectations based on millilensing is observed in the optical or X-rays, and the results are overwhelmingly more compatible with stellar microlensing. We therefore take any millilensing effects to be small. In this case, (1) the stellar Einstein radii projected back to the quasar are more nearly comparable in size with the expected quasar emission regions, thereby allowing for a probe of the inner regions of their accretion disks; (2) variations in the flux ratio anomalies with time in one source, or from source to source, can

provide a direct measure of the dark-to-stellar matter ratios at projected radial distances of  $\sim 2$ – $6$  kpc in elliptical galaxies; and (3) the flux ratio anomalies are expected to vary dramatically on timescales as short as a few years. We note in passing that item (1) above works because microlensing, in effect, is the most powerful zoom lens in astronomy, probing angular sizes down to  $\sim 10^{-6}$  arcsec, which is a factor of  $\sim 10$  better than even Very Long Baseline Interferometry (VLBI) at millimeter wavelengths.

Recently, we have systematically analyzed 10 quadruply imaged quasars using *Chandra X-ray Observatory* archival data and *Hubble Space Telescope* visible images (Pooley et al. 2007). We find that the flux ratio anomalies in the X-ray images of quads are systematically larger than for the same quads imaged in the visible by a factor of  $\sim 2$ . As expected from the models (see Schechter & Wambsganss 2002; Pooley et al. 2007), it is the highly magnified saddle-point image among the four images that is most susceptible to stellar microlensing. Pooley et al. (2007) concluded that the extent (i.e., the half-light radius) of the quasar accretion disks in the optical (i.e.,  $r_{\text{opt}}$ ) must be comparable with (i.e.,  $\gtrsim 1/3$ ) the Einstein radii,  $r_{\text{Ein}}$ , of the stellar microlenses in order to reduce the flux ratio anomalies by the factor of  $\sim 2$  observed. This conflicts with values of  $r_{\text{opt}}$  calculated from simple accretion-disk models, which are expected to be considerably smaller than the Einstein radii, with typical ratios of  $r_{\text{opt}}/r_{\text{Ein}}$  in the range of only 0.01–0.3, with a median value of 0.04 (Pooley et al. 2007).<sup>5</sup> Other studies of individual quad lenses—RX J1131–1231 (Blackburne et al. 2006; Kochanek et al. 2007) and PG 1115+080 (Pooley et al. 2006; Morgan et al. 2008)—have come to similar conclusions. Thus, the observationally inferred optical emission regions in quasars, based on microlensing, are larger than anticipated. This is an intriguing mystery to be pursued. In this regard, we note that the chromatic effect on source size seen in Pooley et al. (2007) has been used to study quasar accretion disk temperature profiles (Poindexter et al. 2008; Anguita et al. 2008), and flatter

<sup>5</sup> These values were reached assuming a mean mass of the microlensing stars of  $0.7 M_\odot$ . For a mean microlensing mass of  $0.3 M_\odot$  (see below), these values should be increased by  $\sqrt{0.7/0.3} = 1.5$ .

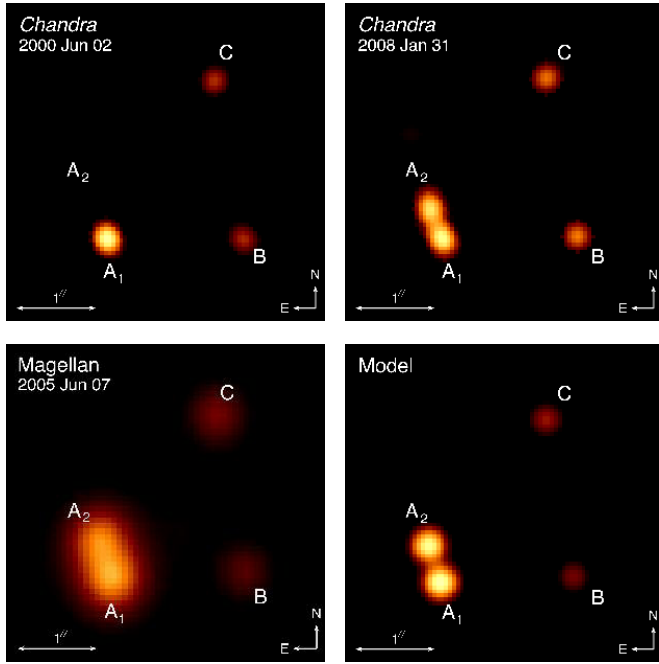


**Figure 1.** Images of PG 1115+080. Clockwise from upper left: maximum-likelihood reconstructed *Chandra* image from 2000, smoothed by a Gaussian; maximum-likelihood reconstructed *Chandra* image from 2008, smoothed by a Gaussian; expected image predicted from singular isothermal sphere plus shear model of lensing galaxy; Magellan  $i'$ -band image. Each image is  $4'' \times 4''$ . The apparent lack of any X-ray emission from  $A_2$  in 2000 is an artifact of the maximum-likelihood reconstruction.

profiles may help resolve the puzzle of the oversized optical accretion disks.

Of equal astrophysical significance, the same observations of the amplitudes and frequency of occurrence of X-ray flux ratio anomalies can also be used to infer the fraction of dark matter at distances from the center of the lensing elliptical galaxies corresponding to the impact parameter of the images (typically  $\sim 2\text{--}6$  kpc; Schechter & Wambsganss 2004). Kochanek and collaborators have pursued this line of investigation using time series of individual lenses to derive dark-matter fractions for several systems (see above; in addition, for work on HE 1104–1805 see Chartas et al. 2008). In this paper, we explore the dark-matter fraction for the galaxy lensing PG 1115+080 using a somewhat different approach. In particular, we describe a new *Chandra* observation of PG 1115+080 in January 2008 which indicates that the  $A_2$  image has dramatically brightened in X-rays compared to its state in 2000 (see Figure 1). In Section 2.1, we review prior optical and X-ray observations of PG 1115+080, while in Section 2.2 we present the new *Chandra* observations and describe the analysis by which we determined the flux ratios. In Section 3, we discuss how inferences about the dark-to-stellar matter ratio can be made from observations of microlensing. Finally, in Section 4 we summarize our results.

## 2. OBSERVATIONS OF PG 1115+080

### 2.1. Prior Observations of PG 1115+080

PG 1115+080 was the second gravitationally lensed quasar to be discovered (Weymann et al. 1980) and the first one found to be quadruple. It has been the subject of numerous studies at wavelengths ranging from radio to mid-infrared to optical to UV to X-ray. It was the first gravitational lens to yield multiple

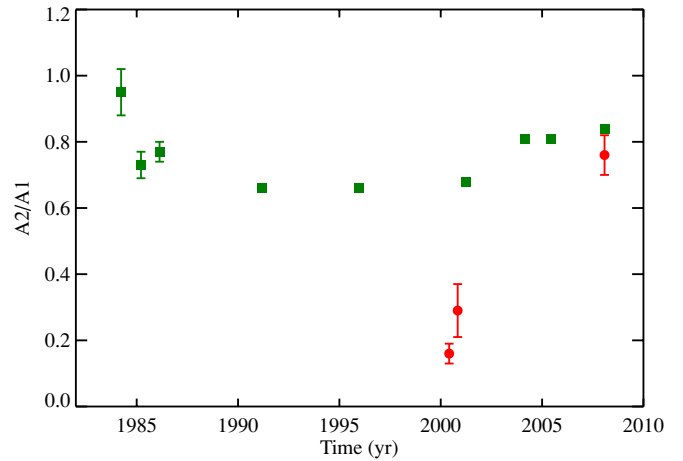


**Figure 2.** Long-term history of the flux ratio  $A_2/A_1$  of PG 1115+080, in the optical band (green squares) and in the X-ray band (red circles). For some of the observations, the plotted error bars are smaller than the plotting symbols. Optical date comes from Vanderriest et al. (1986), Christian et al. (1987), Kristian et al. (1993), Schechter et al. (1997), Pooley et al. (2006), and J. A. Blackburne et al. (2009, in preparation).

**Table 1**  
PG 1115+080 Lens Galaxy Model Parameters

Image	Convergence $\kappa$	Shear $\gamma$	Macromagnification $\mu$
$A_1$	0.537	0.405	+19.7
$A_2$	0.556	0.500	−18.9
$B$	0.658	0.643	−3.37
$C$	0.472	0.287	+5.09

time delays (Schechter et al. 1997), and it shows uncorrelated variations among its images (Foy et al. 1985). The brightest pair of images,  $A_1$  and  $A_2$ , is quite close ( $\sim 0.5''$ ), and simple lens models have these two images resulting from a “fold” caustic. In such cases (Keeton et al. 2005), one expects the two images to be very nearly equal in brightness.

From its discovery more than a quarter century ago to the present, the optical flux ratio between images  $A_2$  and  $A_1$  has been in the range of  $\sim 0.65\text{--}0.85$  as determined from numerous measurements (see Figure 2), and Vanderriest et al. (1986) reported  $A_2/A_1$  varying by  $\sim 30\%$  on a timescale of one year via measurements taken on electronographic plates. Chiba et al. (2005) found that  $A_2/A_1$  is nearly unity in the mid-IR. The nominal flux ratio from the lens model is  $A_2/A_1 = 0.96 \pm 0.05$ . In the course of our investigation of PG 1115+080, we have used two different models for the lensing galaxy. Pooley et al. (2006) used a singular isothermal sphere along with a second isothermal sphere to the west–southwest, approximately where a second galaxy is visible. This model gives an  $A_2/A_1$  ratio of 0.96. In a uniform study of 10 quadruply lensed quasars, Pooley et al. (2007) used a singular isothermal sphere with an external shear, which gives an  $A_2/A_1$  ratio of 0.92. The first model, with two isothermal spheres, has a lower chi-square and explicitly takes into account the environment of the lens galaxy, so we favor it. The convergence  $\kappa$  and shear  $\gamma$  for each of the four images are given in Table 1. The above uncertainty in the model ratio of 0.05 is our nonrigorous estimate for the range of values that reasonable lens models would give.

Thus, the optical flux ratio anomaly is slight, and nearly constant in time (see Figure 2). By sharp contrast, the first two *Chandra* observations in 2000 yielded X-ray ratios of  $A_2/A_1 = 0.16 \pm 0.03$  and  $0.29 \pm 0.08$ , with the  $A_2$  component dramatically

demagnified.<sup>6</sup> Later *XMM* observations of PG 1115+080 (which could not resolve the individual quasar images) showed an overall increase in the X-ray flux of the system, which Pooley et al. (2006) speculated could be due to the brightening of  $A_2$ . This became the motivation for undertaking the *Chandra* observation reported here.

### 2.2. 2008 *Chandra* Observation of PG 1115+080

PG 1115+080 was observed for 28.8 ks on 2008 January 31 (ObsID 7757) with the Advanced CCD Imaging Spectrometer (ACIS). The data were taken in timed-exposure mode with an integration time of 3.24 s per frame, and the telescope aim point was on the backside-illuminated S3 chip. The data were telemetered to the ground in very faint mode.

Reduction was performed using the CIAO 4.0 software provided by the *Chandra* X-ray Center. The data were reprocessed using the CALDB 3.4.3 set of calibration files (gain maps, quantum efficiency, quantum efficiency uniformity, effective area) including a new bad pixel list made with the `acis_run_hotpix` tool. The reprocessing was done without including the pixel randomization that is added during standard processing. This omission slightly improves the point-spread function (PSF). The data were filtered using standard event grades and excluding both bad pixels and software-flagged cosmic-ray events. No intervals of strong background flaring were found. No pileup correction was made.

Our analysis follows the procedure laid out in Pooley et al. (2007). We produced a 0.3–8 keV image of PG 1115+080 with a resolution of  $0.0246'' \text{ pixel}^{-1}$ . To determine the intensities of each lensed quasar image, a two-dimensional model consisting of four Gaussian components plus a constant background was fitted to the data. The background component was fixed to a value determined from a source-free region near the lens. The relative positions of the Gaussian components were fixed to the separations determined from *Hubble Space Telescope* observations (Kristian et al. 1993), but the absolute position was allowed to vary. Each Gaussian was constrained to have the same full width at half-maximum, but this value was allowed to float. The fit was performed with Sherpa 3.4 using Cash (1979) statistics and the Powell minimization method. From this fit, we measure the value of  $A_2/A_1$  to be  $0.76 \pm 0.06$ , very near to the optical flux ratio.

In order to visualize the dramatic rise in the flux of  $A_2$  (with the  $A_2$  and  $A_1$  images clearly separated), we produced maximum-likelihood reconstructions of two *Chandra* images from the 2000 and 2008 observations. For this, we used the `max_likelihood` function in the IDL Astronomy User's Library, which is based on the algorithms of Richardson (1972) and Lucy (1974). This is a simple, iterative, Bayesian technique to estimate the deconvolution of the observed data and the instrumental PSF. The PSF was constructed using the *Chandra* Ray Tracer (ChaRT) to produce a simulated PSF and Marx 4.3<sup>7</sup> to project the PSF onto the detector. *Chandra*'s PSF is energy dependent, and we extracted the spectrum of PG 1115+080 to provide the appropriate input to ChaRT. With this simulated

<sup>6</sup> This extreme anomaly is very similar to the case of SDSS 0924+0219 in the optical (Keeton et al. 2006; Pooley et al. 2006). The arrangement of the images is virtually identical in the two systems. However, SDSS 0924+0219 differs from PG 1115+080 and most other quadruply lensed quasars in that it harbors a relatively small black hole. The smaller physical scale of the accretion disk in SDSS 0924+0219 may play a role in explaining the anomalous flux ratios of its emission lines (Keeton et al. 2006), which may come from a region small enough to be affected by microlensing—as the optical continuum is (Morgan et al. 2006)—as well as by millilensing.

<sup>7</sup> <http://space.mit.edu/ASC/MARX/>

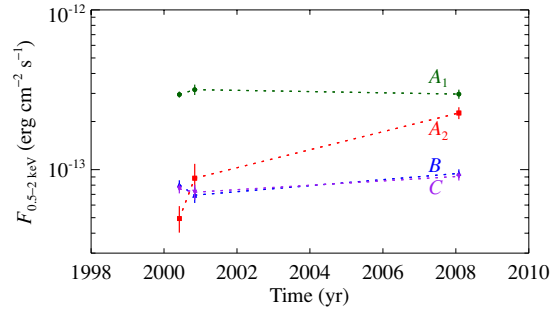


Figure 3. X-ray fluxes vs. time of the individual images of PG 1115+080.

Table 2  
X-Ray Fluxes of PG 1115+080 Images

Date	$F_x$ ( $10^{-14}$ erg cm $^{-2}$ s $^{-1}$ )			
	$A_1$ (HM)	$A_2$ (HS)	$B$ (LS)	$C$ (LM)
2000 Jun 2	$29.5 \pm 1.3$	$4.94 \pm 0.94$	$8.04 \pm 0.53$	$7.58 \pm 0.50$
2000 Nov 3	$31.7 \pm 2.4$	$8.84 \pm 2.0$	$6.92 \pm 0.77$	$7.22 \pm 0.79$
2008 Jan 31	$29.7 \pm 2.0$	$22.6 \pm 1.9$	$9.47 \pm 0.56$	$9.08 \pm 0.54$

Note. HM: high-magnification minimum image; HS: high-magnification saddle-point image; LS: low-magnification saddle-point image; LM: low-magnification minimum image.

PSF of PG 1115+080, we performed 1000 iterations of the `max_likelihood` function on the data and smoothed the result with a Gaussian for aesthetic reasons. The results are shown in Figure 1, along with a Magellan  $i'$ -band image and an image using four Gaussians to represent the expected image based on our model. The apparent lack of any emission from  $A_2$  in 2000 is an artifact of the Lucy–Richardson deconvolution, which does not seem to robustly handle faint sources (e.g.,  $A_2$ ) in the immediate vicinity of much brighter sources (e.g.,  $A_1$ ).

The long-term history of the  $A_2/A_1$  flux ratio in the optical and X-ray is summarized in Figure 2. The X-ray history of the fluxes from each of the quasar images, based on our two-dimensional Gaussian fits and the measured spectrum of image C, is given in Table 2 and displayed in Figure 3, showing that the change in  $A_2/A_1$  is indeed a result of  $A_2$  becoming less demagnified. The fluxes of image C given in Table 2 are slightly different than those reported in Pooley et al. (2007) because we are now simultaneously fitting the source and background spectra using the statistics of Cash (1979) rather than fitting background-subtracted spectra using  $\chi^2$  statistics. The flux ratios are unchanged.

### 3. EVALUATION OF DARK-TO-STELLAR MATTER CONTENT

The way in which observations of flux ratio anomalies, and their variations with time, can lead to an estimate of the dark-to-stellar matter content of the lensing elliptical galaxy is based on analyses of stellar microlensing magnification maps (Wambsganss 1999). The magnification distributions change with the addition of smooth matter but in ways that are sometimes counterintuitive. The case of the  $A_1$  and  $A_2$  images in PG 1115+080 is close to that considered by Schechter & Wambsganss (2002), with the magnification distributions getting broader (sometimes even bifurcating) and growing more asymmetric as one dilutes a pure stellar population with uniformly distributed dark matter. An illustrative magnification map for a lensing galaxy with 80% smoothly distributed dark matter and 20% stars is shown in Figure 4. This map (like all the maps we used) is  $2000 \times 2000$  pixels, with an outer scale of

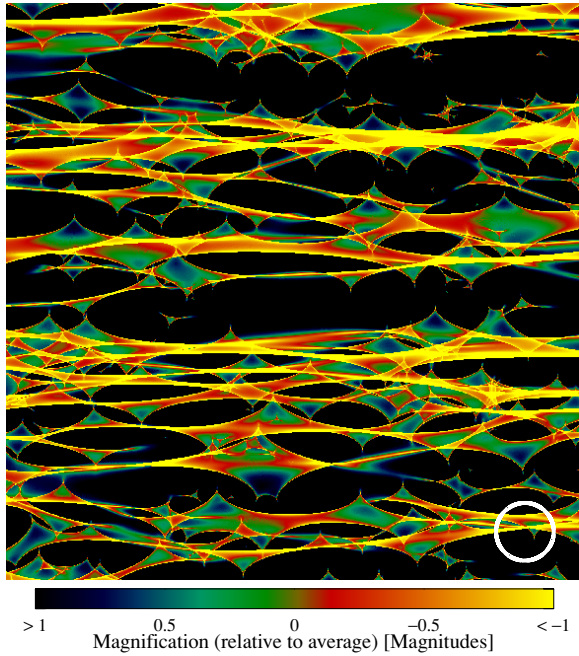


**Figure 4.** Sample magnification map for an overall lensing potential which includes 80% dark matter and a 20% contribution from stars (for a negative parity image region with a mean magnification of 12). This map represents a tiny section of the lensing galaxy that is  $\sim 28 \mu\text{s}$  ( $20 r_{\text{Ein}}$ ) on a side, and is presented with a logarithmic display with the log of the *mean magnification* of the galaxy subtracted off. The white circle has a radius equal to the Einstein radius of a stellar microlens.

$20 r_{\text{Ein}}$  and a pixel size of  $0.01 r_{\text{Ein}}$ . All of the stars have the same mass, which we take to be  $0.3 M_{\odot}$ .<sup>8</sup> This type of magnification map is constructed in the source plane, and its center is referenced to the location of one of the quad images. It shows the effects of microlensing magnification (due to the sum of all the microimages) for a source location anywhere within the map. For the visual presentation of the map, the mean magnification, due to the smooth lensing potential, has been subtracted off. The particular example shown in Figure 4 is for a highly magnified saddle (HS) point image (e.g.,  $A_2$  in PG 1115+080). The sharp-edged features in Figure 4 correspond to caustics, the crossing of which by the source corresponds to the creation or annihilation of microlensing image pairs. Such magnification maps have also been generated so as to additionally represent the high-magnification minimum (HM), low-magnification saddle (LS), and low-magnification minimum (LM) images ( $A_1$ ,  $B$ , and  $C$ , respectively).

We approach the magnification map analyses in three slightly different and complementary ways, described and discussed below.

### 3.1. Bayesian Analysis I

The distributions of magnifications produced from such maps, for two different values of dark-to-stellar matter ratios, are shown in the top panels of Figure 5 (the histograms have been shifted, which we describe below). The different colored histograms in each panel are for the HS, HM, LS, and LM images.

<sup>8</sup> The value of  $\langle M \rangle \simeq 0.3 M_{\odot}$  is derived from a stellar-mass function taken from Kroupa et al. (1993; their Equation (13)), weighted by an additional factor of  $M^{1/2}$  to take into account the dependence of the linear size of the microlensing Einstein radius on  $M^{1/2}$ . The averaging is done for the mass range  $0.02 < M < 1 M_{\odot}$ ; a slightly larger value is obtained for the mass range  $0.08 < M < 1 M_{\odot}$ , where the Kroupa et al. (1993) mass function is strictly applicable.

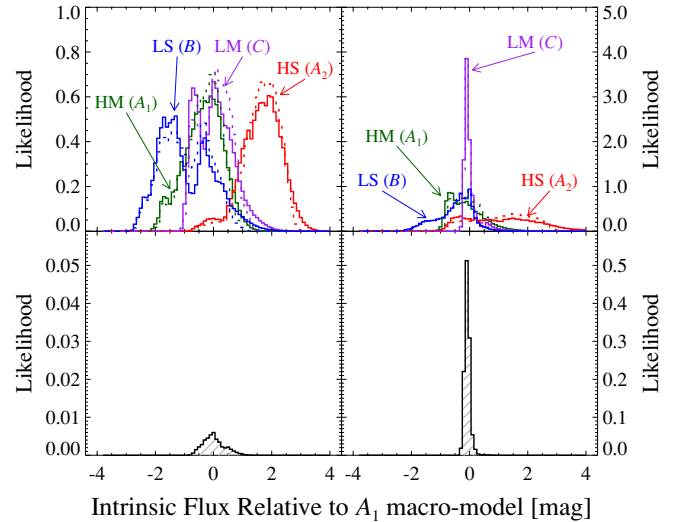


**Figure 5.** Illustrative likelihood analysis for estimating the dark-to-stellar matter fraction. Top panels: distributions expressing the likelihood of having an intrinsic X-ray source intensity, given the observed X-ray intensity. The different colors are for the HS, HM, LS, and LM quad images (see the text). The intensities are given in magnitude units. The left panel is for a model where 100% of the matter is in the form of stars; the right panel is for the case of 90% dark matter and 10% stars. The histograms have each been shifted so that the zero point corresponds to the observed intensity, normalized to the smooth lens model value. The solid lines correspond to the X-ray emitting region being a point-source, and the dotted lines correspond to the X-ray emitting region having an effective half-light radius of  $\log_{10}(r_x/\text{cm}) = 15.6$  (Morgan et al. 2008). Bottom panels: distributions expressing the likelihood of having an intrinsic X-ray source intensity after taking into account the observed intensity of all four images combined. Note the difference in scale between the left and right vertical axes. We plot only the results for a point source because the curves for the extended model are indistinguishable. See the text and Figure 6 for the results for other dark matter-to-star ratios.

These histograms represent  $\mathcal{P}(O|I)$ , which is the probability that if the source (the quasar) has an intrinsic intensity  $I$  (i.e., in the absence of microlensing), an intensity  $O$  will be observed (as modified by microlensing). By Bayes' Theorem, this posterior probability is proportional to the likelihood that the intrinsic intensity is  $I$  if we observe intensity  $O$ .

We treat the histograms in Figure 5 as likelihood distributions of the intrinsic source intensity, given the observed fluxes of the four individual images (during the June 2000 observation). Without loss of generality, we take the zero point to be the intrinsic source intensity such that the observed flux for image  $A_1$  is exactly as predicted by the macromodel for PG 1115+080. The histograms for the other images have been shifted by  $[(m_j^{\text{obs}} - m_{A_1}^{\text{obs}}) - (m_j^{\text{macro}} - m_{A_1}^{\text{macro}})]$ ,  $j \in (A_2, B, C)$ , to account for the fact that the observed magnitude differences do not agree with the macromodel magnitude differences and therefore must be microlensed. The largest shift is for the HS image (i.e.,  $A_2$  which was highly demagnified in 2000). We then find the combined likelihood of an intrinsic intensity  $I$  for all four images by taking the product of the (shifted) set of histograms. The results are shown in the bottom panels of Figure 5 as likelihood distributions as a function of the intrinsic intensity of the source. The area under the likelihood curve for the model with 100% stars is an order of magnitude smaller than for the model with only 10% stars (i.e., 90% dark matter).

We have repeated the same calculations for nine different stellar mass fractions. The results are shown in Figure 6 as relative likelihood plotted against stellar fraction. Note that the scale of stellar fraction is not linear. From this result, we conclude that the most likely fraction of mass in stars in the

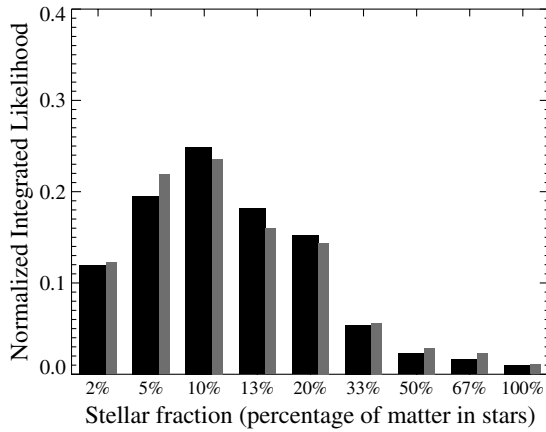


**Figure 6.** Likelihood histogram of the dark-matter fraction based on the first maximum likelihood analysis described in the text, normalized such that each set of values adds to unity. The thicker, black bars correspond to the point-source analysis, and the thinner, gray bars correspond to the analysis in which the X-ray emitting region has a half-light radius of  $\log_{10}(r_x/\text{cm}) = 15.6$ .

lensing galaxy at the typical impact parameter of the four lensed images ( $\sim 5$  kpc) is  $\sim 10\%$ .

The above analysis assumed that the X-ray emitting region of PG 1115+080 is effectively a point source, i.e., very small with respect to the size of 1 pixel. Morgan et al. (2008) estimated that the X-ray region has an effective half-light radius of  $\log_{10}(r_x/\text{cm}) = 15.6^{+0.6}_{-0.9}$ . We explore the effects of such a finite-size source with  $\log_{10}(r_x/\text{cm}) = 15.6$  by convolving the microlensing magnification maps with a two-dimensional Gaussian with  $\sigma = r_x/\sqrt{2} \log 2 = 9.2$  pixels and then repeating the histogram analysis. The results are indicated by the dotted lines in Figure 5 and the gray bars in Figure 6.

### 3.2. Bayesian Analysis II

We take a slightly different approach here to mitigating our ignorance of the intrinsic intensity of the source. We perform an analysis based on each image’s fraction of the total observed intensity (which is based on our two-dimensional fitting described in Section 2.2). The total model intensity is obtained by multiplying the microlensing map for each

image by its macromagnification and adding the resultant four maps together. We then form fractional intensity maps by dividing the individual microlensing maps (multiplied by their macromagnification) by the total intensity map.

We use Bayes’s theorem to calculate

$$P(\text{stellar fract}_i | f_{j,2000}) = \frac{P(f_{j,2000} | \text{stellar fract}_i) P(\text{stellar fract}_i)}{P(f_{j,2000})}, \quad (1)$$

where  $f_{j,2000}$  is the observed flux (expressed as a fraction of the total intensity) of image  $j \in (A_1, A_2, B, C)$  in the 2000 observation and stellar fract $_i$  is the stellar fraction for which a particular microlensing map (and its associated fractional intensity map) is generated. We discuss each of the three terms on the right-hand side.

The term  $P(f_{j,2000} | \text{stellar fract}_i)$  represents the probability to obtain the observed flux in 2000 for a specific stellar fraction. To calculate this, we count all pixels in the fractional intensity map for that stellar fraction which lie within the  $1\sigma$  confidence interval of  $f_{j,2000}$  (e.g.,  $f_{A_2,2000} = 0.10 \pm 0.02$ ) and divide by the total number of pixels in the map.

The term  $P(\text{stellar fract}_i)$  is the prior probability on a specific stellar fraction, which we take to be uniform. All of these values are therefore  $1/9$ .

The denominator,  $P(f_{j,2000})$ , is similar to the first term but without regard to any particular stellar fraction. We calculate this by counting the number of pixels in all maps that lie within the  $1\sigma$  confidence interval of  $f_{j,2000}$  and dividing by the total number of pixels in all maps.

Using this framework, we calculate the posterior probability of each stellar fraction based on each value of  $f_j$ . We then multiply those probabilities for each stellar fraction together to produce a plot similar to Figure 6. These results are shown in Figure 7. The probabilities based on the individual images (left panels) show that some of the images have more power to discriminate between the different stellar fractions than others. As expected, the  $A_2$  image strongly favors certain fractions over others, and the  $B$  and (to a lesser extent)  $C$  images also show some power of discrimination. The  $A_1$  image appears roughly equally consistent with any stellar fraction. Combining these individual image analyses, we obtain the right panel of Figure 7.

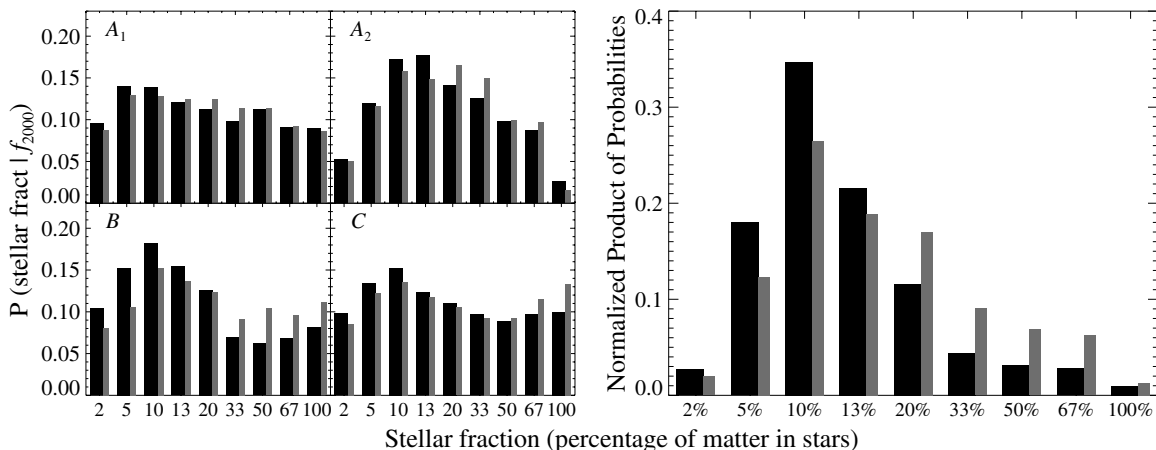


**Figure 7.** Left: the probability of a certain stellar fraction given the observed flux in 2000 for each image, calculated using the second method described in the text. Right: product of these four probabilities for each stellar fraction, normalized such that each set of values adds to unity. In each plot, the thicker, black bars correspond to the point-source analysis, and the thinner, gray bars correspond to the analysis in which the X-ray emitting region has a half-light radius of  $\log_{10}(r_x/\text{cm}) = 15.6$ .

The above analysis assumed that the X-ray emitting region of PG 1115+080 is effectively a point source. As in the previous analysis, we explore the effects of a finite-size source by convolving the microlensing magnification maps with a two-dimensional Gaussian with  $\sigma = 9.2$  pixels (appropriate for  $\log_{10}(r_x/\text{cm}) = 15.6$ ) and then repeating the analysis. The results are indicated by the gray bars in Figure 7.

Because the previous analysis and this one utilize similar methods, one might expect them to yield identical answers. Indeed, the right panel of Figure 7 shows good agreement with the first Bayesian approach, namely, the most likely breakdown of matter in the lensing galaxy at the typical impact parameter of the four images is  $\sim 10\%$  of the matter in stars and  $\sim 90\%$  in a smooth, dark component. The small differences between the two approaches are attributed to the fact that in the second approach the position of the source is the same in all four maps, while in the first approach the source will in general have different positions in the four different maps.

### 3.3. Bayesian Analysis III

The third approach utilizes two epochs of *Chandra* data. We calculate the posterior probability of each stellar fraction given the observations in 2000 and 2008, subject to the constraint that the source and magnification map moved a certain amount relative to each other in the intervening eight years. We start with three components of the velocity:  $94 \text{ km s}^{-1}$  for the motion of the Sun with respect to the cosmic microwave background, projected transverse to PG 1115+080 (Morgan et al. 2008);  $280 \text{ km s}^{-1}$  for the stellar velocity dispersion of PG 1115+080 (Tonry 1998); and  $235 \text{ km s}^{-1}$  for the peculiar velocity dispersion of galaxies (Kochanek 2004). The peculiar velocities are corrected for (1) the decrease in the peculiar velocity field as the universe expands (see prescription in Kochanek 2004), (2) a factor of  $\sqrt{2}$  to correct the one-dimensional velocity dispersions into the two-dimensional plane of the sky, and (3) for time dilation at the source and at the lens (all using the standard  $\Lambda$ CDM cosmology). Similarly, the stellar-velocity dispersion is corrected for effects (2) and (3). The velocities are then converted to angular velocities, taking into account the angular diameter distances to the source (1800 Mpc) and the lens (930 Mpc). Finally, the angular velocities are added appropriately in quadrature. The result for PG 1115+080 is an rms angular motion of  $0.10 \mu\text{as yr}^{-1}$ . If we allow for some uncertainty in the assumed dispersion velocities of  $50 \text{ km s}^{-1}$  (at the source and at the lens), then the range in rms angular motion is  $0.08\text{--}0.12 \mu\text{as yr}^{-1}$ . In the 2800 days between the 2000 and 2008 *Chandra* observations of PG 1115+080, this corresponds to a range of rms angular motions of  $0.77 \pm 0.15 \mu\text{as}$ . For the same cosmology, the Einstein radius of a  $0.3 M_{\odot}$  microlens in the lensing galaxy would be  $r_{\text{Ein}} \simeq 1.4 \mu\text{as}$ . Thus, the relative motion of the source and the map is  $0.45\text{--}0.67 r_{\text{Ein}}$  (see Figure 4). This angular distance would be approximately a full Einstein radius for a  $2\sigma$  realization of the rms motions (see Figure 4).

We use Bayes's theorem to calculate

$$\begin{aligned} & P(\text{stellar fract}_i | f_{j,2000} \cap f_{j,2008}) \\ &= P(f_{j,2008} | \text{stellar fract}_i \cap f_{j,2000}) \frac{P(\text{stellar fract}_i | f_{j,2000})}{P(f_{j,2008} | f_{j,2000})}. \end{aligned} \quad (2)$$

We again discuss the three terms on the right-hand side.

The term  $P(f_{j,2008} | \text{stellar fract}_i \cap f_{j,2000})$  represents the probability to obtain the observed fractional intensity in 2008 for a specific stellar fraction and observed intensity in 2000. To calculate this, we first find all pixels, for a given stellar fraction, in the map which lie within the  $1\sigma$  confidence interval of  $f_{j,2000}$ . Around each of these pixels, we consider an annulus corresponding to our velocity range and the eight year interval between observations; the total number of pixels in all such annuli is  $N_i$ . We also count the number  $M_i$  of these pixels that lie within the  $1\sigma$  confidence interval of  $f_{j,2008}$ , and we calculate  $P(f_{j,2008} | \text{stellar fract}_i \cap f_{j,2000}) = M_i/N_i$ . We take each pixel in the annuli to be equally likely for all four of the images. That is, despite the fact that the source motion is correlated on the four static magnification maps for a given stellar fraction, we allow for random directions in each of the magnification maps, in part, because of the random motions of the individual stars.

The term  $P(\text{stellar fract}_i | f_{j,2000})$  is the left-hand side of Equation (1) and was explained in the previous section.

The denominator,  $P(f_{j,2008} | f_{j,2000})$ , is similar to the first term but without regard to any particular stellar fraction. We simply sum over all maps and calculate this term as  $(\sum_i M_i)/(\sum_i N_i)$ .

Similar to the previous analysis, we calculate the posterior probability of each stellar fraction based on each  $f_j$ . We then multiply those probabilities for each stellar fraction together to produce a plot similar to Figure 7, and this is shown in Figure 8. Comparing this with the previous Bayesian analysis of just the first epoch of data, the most likely stellar fraction (10%) is the same. The addition of the 2008 data appears to have made smaller stellar fractions slightly less likely and larger stellar fractions slightly more likely. We discuss this below.

Again, the above analysis assumed that the X-ray emitting region of PG 1115+080 is effectively a point source. As in the previous two analyses, we also explore the effects of a finite-size source by convolving the microlensing magnification maps with a two-dimensional Gaussian with  $\sigma = 9.2$  pixels (appropriate for  $\log_{10}(r_x/\text{cm}) = 15.6$ ) and then repeating the analysis. The results are indicated by the gray bars in Figure 8.

A more comprehensive approach to multiply sampled light curves has been developed by Kochanek (2004) who then applied it to the case of Q 2237+0305. The locations of the images of this quasar are close to the core of the (barred spiral) lensing galaxy because the lens redshift is low. This makes it much more likely that the quasar has crossed one or more caustics, but it also ensures a higher stellar mass fraction, as was found by Kochanek. Morgan et al. (2008), in a study of PG 1115+080, choose to parameterize their models by a global rather than a local stellar mass fraction. Their likelihood function, while broad, peaks at 0.4. Chartas et al. (2008) carry out a similar analysis for the system HE 1104–1805 and find a global stellar mass fraction of 0.2

### 3.4. Evaluation of the Rapid Temporal Change

We use the stellar microlensing magnification maps to investigate the likelihood that the  $A_2$  image would have changed its intensity by a factor of  $\sim 6$  during an interval of eight years (in the observer frame). We choose this interval because it is the length of time between the first *Chandra* observation of PG 1115+080 and the most recent. *XMM* observations during this interval indicate that the rise in  $A_2$  could have occurred as early as November 2001 (see Figure 3 of Pooley et al. 2006), but the *Chandra* observation in 2008 is the first to show directly that  $A_2$  has brightened. In Figure 9, we plot the probability of finding image  $A_2$  with a fraction  $f_{A_2,2008}$  of the total source intensity in



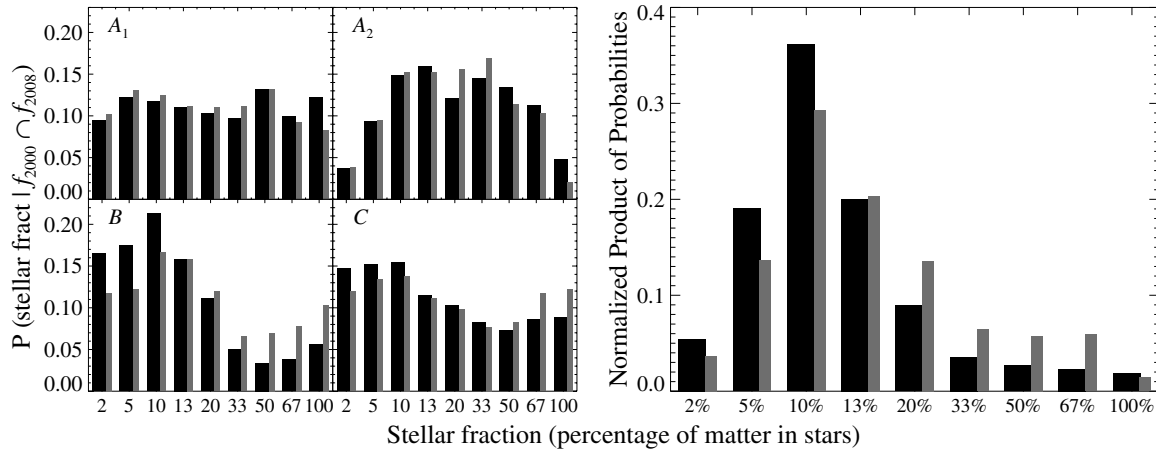


**Figure 8.** Left: the probability of a certain stellar fraction given the observed fluxes in 2000 and 2008 for each image, as calculated using the third method described in the text. Right: product of these four probabilities for each stellar fraction, normalized such that each set of values adds to unity. In each plot, the thicker, black bars correspond to the point-source analysis, and the thinner, gray bars correspond to the analysis in which the X-ray emitting region has a half-light radius of  $\log_{10}(r_x/\text{cm}) = 15.6$ .

2008, given that the fraction in 2000 was  $f_{A_2,2000} = 0.10 \pm 0.02$ . This probability density function is shown for each of the nine stellar fractions that we considered (for both point source and extended source). These functions are computed as described above for  $P(f_{j,2008} | \text{stellar frac}_i \cap f_{j,2000})$  with  $j = A_2$  for a complete range of possible values for  $f_{A_2,2008}$ . As can be seen, it is somewhat unlikely in all cases (i.e.,  $\lesssim 30\%$  probability) to observe such a large rise in  $A_2$  in only eight years—but not implausibly so.

### 3.5. Discussion of the Bayesian Methods

The individual panels of the left-hand side of Figure 7 are essentially another way of looking at the magnification map histograms in the top panels of Figure 5; the panels of Figure 7 show the probabilities of the nine magnification maps to produce the flux fraction that was observed. Whereas all maps (i.e., stellar fractions) can accommodate the  $A_1$  and, to some extent,  $C$  observed values, the  $A_2$  and  $B$  values observed in 2000 are much more likely to have come from stellar fractions of 5%–20%, producing a combined probability that is fairly strongly peaked around a stellar fraction of 10%.

When the additional information that  $A_2$  became much less demagnified on a timescale of eight years is added, the combined probability becomes somewhat less strongly peaked. The individual panels on the left-hand side of Figure 8 show that, in comparison to the 2000 data alone, this difference is due mainly to the difference in the  $A_2$  probability distribution, which in this case is roughly equally probable to come from a stellar fraction of 10% as 67%. We interpret this as a reflection of the relatively higher probability to cross a caustic on such a short timescale in high-stellar-fraction magnification maps; in low-stellar-fraction magnification maps, the caustics are too few and far between. Put another way, there is a tradeoff between having a low enough stellar density to give a high probability to find  $A_2$  in a demagnified state (in 2000) and having a high enough stellar density to have enough caustics that  $A_2$  can become brightened on a short timescale (in 2008). For example, Figure 9 shows that, although all stellar fractions give a relatively low probability of observing such a dramatic change in  $A_2$  in only eight years, the highest stellar fractions give a higher probability of such a change.

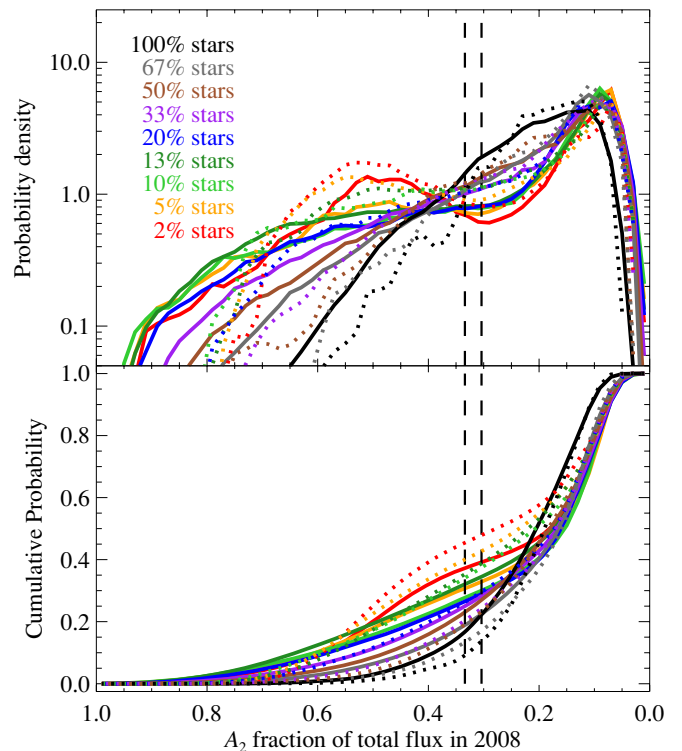


**Figure 9.** Probability density (top) and cumulative probability (bottom) of  $A_2$  fractional flux in 2008 given the value in 2000. The solid lines correspond to the point-source analysis, and the dotted lines correspond to the analysis in which the X-ray emitting region has a half-light radius of  $\log_{10}(r_x/\text{cm}) = 15.6$ . The vertical dashed lines mark the  $1\sigma$  confidence intervals of the measured value in 2008.

If the relative motion between the source and the magnification map were much larger, it would be easier to accommodate both the 2000 and 2008 observations of  $A_2$  with the low-stellar-fraction maps, as it would be if the temporal baseline were much larger, which it very well could be. Figure 3 of Pooley et al. (2006) shows that, based on the unresolved total flux, it is likely that  $A_2$  was demagnified in all previous X-ray observations except the first observation by *Einstein* in December 1979

which showed a total flux from PG 1115+080 comparable to that of the first *XMM* observation in 2001 November. Although the X-ray light curve is sparsely sampled, and although *Chandra* is the only instrument which can separately measure the individual images, it is possible that  $A_2$  was in a demagnified state for  $\sim 22$  years. This would certainly change the results in Figure 9, for the probability of such a dramatic change in  $A_2$ , but would leave the basic conclusions regarding the stellar mass fraction intact.

In addition to the uncertainties in baselines (due to sparsely sampled light curves) and relative velocities, there is another shortcoming to this type of Bayesian analysis, namely, the use of static magnification maps to analyze temporal behavior. As shown by Kundic & Wambsganss (1993) and Wambsganss & Kundic (1995), the motions of the individual stars in the lensing galaxy can cause shorter and more frequent microlensing events than bulk motion can produce, by perhaps a factor of two. Unlike the present case, the magnification maps they used had zero shear. A preliminary reconnaissance of maps with shear equal to the convergence, appropriate to isothermal potentials, and with 10%–20% of the mass in stars, indicates that allowing for the motion of individual stars would again produce changes on a timescale only a factor of two shorter.

Given the additional complications introduced by the relative motions between the quasar and the microlensing stars, the first and second Bayesian analyses are clearly more straightforward, free from the uncertainties in the third. In a forthcoming paper, we will apply the first method to 14 quadruply lensed quasars that *Chandra* has observed (D. Pooley et al. 2009, in preparation).

Finally, we point out one common feature of all three approaches: the important role that the low-magnification images ( $B$  and  $C$ ) play in constraining the stellar fraction. This is evident in the individual panels of Figures 8 and 7. It can also be seen in the upper panels of Figure 5 by considering the effects of the LM and LS histograms (their peaks and their cutoffs) on the final product.

The above analyses are based on the assumption that the mass profile of the lensing galaxy is nearly isothermal, as appears to be nearly universally so for the Sloan Lens ACS Survey (SLACS) sample of galaxies lensed by bright elliptical galaxies (Bolton et al. 2008). There is, however, evidence from time delays (Schechter et al. 1997) and from a stellar velocity dispersion (Tonry 1998) that PG 1115+080 is unusual in having mass follow light. In our view, the purely geometric-argument determinations by the SLACS group are more reliable than either time delays or velocity dispersion measurements, but the possibility remains that PG 1115+080 is different and that we have used a somewhat inappropriate model. We address this point further in a forthcoming paper (P. L. Schechter et al. 2009, in preparation).

#### 4. SUMMARY AND CONCLUSIONS

We have observed a dramatic change in the X-ray flux of the  $A_2$  image of PG 1115+080 in *Chandra* observations that were separated by eight years. The short timescale for the flux change clearly indicates the presence of stellar microlensing rather than millilensing due to dark matter substructure in the elliptical lensing galaxy. The observations of the fluxes of the individual images point toward a substantial dark matter fraction of  $\sim 80\%$ – $95\%$  at a distance of  $\sim 6$  kpc from the galaxy center.

One particularly interesting aspect of the observed change in flux ratio between the  $A_2$  and  $A_1$  images is the very rapid timescale on which it occurred ( $\sim$ eight years). For typical expected transverse angular velocities of  $\sim 0.1 \mu\text{as yr}^{-1}$  it seems somewhat unlikely that the source will start on a point of very low magnification (see, e.g., Figure 4) and end up. With an unexpectedly high angular velocity of  $\sim 0.2 \mu\text{as yr}^{-1}$  the likelihood for the observed change in magnification of the  $A_2$  image becomes considerably greater. In this regard, we note that the recent report of an even larger change in a flux ratio in the quad lens RX J1131–1231 over an interval of  $\sim$ two years (Chartas et al. 2008) indicates that the variation that we observed in PG 1115+080 is perhaps not a rare occurrence. The difference between the effect of bulk and random motion of the microlensing stars is probably not sufficient to account for these rapid variations, leaving us with an unresolved puzzle.

D.P. thanks Nicholas E. Matsakis and Eric M. Downes for extremely useful discussions of Bayesian analysis and is grateful to the MIT Kavli Institute for Astrophysics and Space Research for its hospitality during the summer of 2008 during which most of this work was done. D.P. and S.R. gratefully acknowledge support from *Chandra* grants G07-8098A&B. J.A.B. and P.L.S. acknowledge support from US NSF grant AST-0607601.

#### REFERENCES

- Anguita, T., Schmidt, R. W., Turner, E. L., Wambsganss, J., Webster, R. L., Loomis, K. A., Long, D., & McMillan, R. 2008, *A&A*, **480**, 327
- Blackburne, J. A., Pooley, D., & Rappaport, S. 2006, *ApJ*, **640**, 569
- Bolton, A. S., Treu, T., Koopmans, L. V. E., Gavazzi, R., Moustakas, L. A., Burles, S., Schlegel, D. J., & Wayth, R. 2008, *ApJ*, **684**, 248
- Cash, W. 1979, *ApJ*, **228**, 939
- Chartas, G., Kochanek, C. S., Dai, X., Poindexter, S., & Garmire, G. 2008, arXiv:0805.4492
- Chiba, M. 2002, *ApJ*, **565**, 17
- Chiba, M., Minezaki, T., Kashikawa, N., Kataza, H., & Inoue, K. T. 2005, *ApJ*, **627**, 53
- Christian, C. A., Crabtree, D., & Waddell, P. 1987, *ApJ*, **312**, 45
- Dalal, N., & Kochanek, C. S. 2002, *ApJ*, **572**, 25
- Foy, R., Bonneau, D., & Blazit, A. 1985, *A&A*, **149**, L13
- Keeton, C. R., Burles, S., Schechter, P. L., & Wambsganss, J. 2006, *ApJ*, **639**, 1
- Keeton, C., Gaudi, B., & Petters, A. 2005, *ApJ*, **635**, 35
- Kochanek, C. S. 2004, *ApJ*, **605**, 58
- Kochanek, C. S. 2006, Saas-Fee Advanced Course 33: Gravitational Lensing: Strong, Weak and Micro, ed. G. Meylan, P. Jetzer, & P. North (Berlin: Springer), 91
- Kochanek, C. S., Dai, X., Morgan, C., Morgan, N., & Poindexter, S. C. G. 2007, ASP Conf. Ser. 371, Statistical Challenges in Modern Astronomy IV, ed. G. J. Babu & E. D. Feigelson (San Francisco, CA: ASP), 43
- Kochanek, C. S., & Dalal, N. 2004, *ApJ*, **610**, 69
- Kristian, J., et al. 1993, *AJ*, **106**, 1330
- Kroupa, P., Tout, C. A., & Gilmore, G. 1993, *MNRAS*, **262**, 545
- Kundic, T., & Wambsganss, J. 1993, *ApJ*, **404**, 455
- Lucy, L. B. 1974, *AJ*, **79**, 745
- Mao, S., & Schneider, P. 1998, *MNRAS*, **295**, 587
- Metcalf, R. B., & Madau, P. 2001, *ApJ*, **563**, 9
- Metcalf, R. B., & Zhao, H. 2002, *ApJ*, **567**, L5
- Morgan, C. W., Kochanek, C. S., Dai, X., Morgan, N. D., & Falco, E. E. 2008, *ApJ*, **689**, 755
- Morgan, C. W., Kochanek, C. S., Morgan, N. D., & Falco, E. E. 2006, *ApJ*, **647**, 874
- Poindexter, S., Morgan, N., & Kochanek, C. S. 2008, *ApJ*, **673**, 34
- Pooley, D., Blackburne, J. A., Rappaport, S., & Schechter, P. L. 2007, *ApJ*, **661**, 19
- Pooley, D., Blackburne, J. A., Rappaport, S., Schechter, P. L., & Fong, W.-f. 2006, *ApJ*, **648**, 67
- Richardson, W. H. 1972, *J. Opt. Soc. Am.*, **62**, 55

- Schechter, P. L., & Wambsganss, J. 2002, *ApJ*, **580**, 685
- Schechter, P. L., & Wambsganss, J. 2004, in IAU Symp. 220, ed. S. D. Ryder, D. J. Pisano, M. A. Walker, & K. C. Freeman (Dordrecht: Kluwer), 103 (arXiv:astro-ph/0309163)
- Schechter, P. L., et al. 1997, *ApJ*, **475**, L85
- Tonry, J. L. 1998, *AJ*, **115**, 1
- Vanderriest, C., Wlerick, G., Lelievre, G., Schneider, J., Sol, H., Horville, D., Renard, L., & Servan, B. 1986, *A&A*, **158**, L5
- Wambsganss, J. 1999, *J. Comput. Appl. Math.*, **109**, 353
- Wambsganss, J. 2006, in Saas-Fee Advanced Course 33, Gravitational Lensing: Strong, Weak and Micro, ed. G. Meylan, P. Jetzer, & P. North (Berlin: Springer), 453
- Wambsganss, J., & Kundic, T. 1995, *ApJ*, **450**, 19
- Wambsganss, J., & Paczyński, B. 1992, *ApJ*, **397**, L1
- Weymann, R. J., et al. 1980, *Nature*, **285**, 641
- Witt, H., Mao, S., & Schechter, P. L. 1995, *ApJ*, **443**, 18